Materials Research Express

PAPER • **OPEN ACCESS**

Formation and stability of Fe-rich terminations of the $Fe_3O_4(001)$ surface

To cite this article: Oscar Gamba *et al* 2023 *Mater. Res. Express* **10** 116517

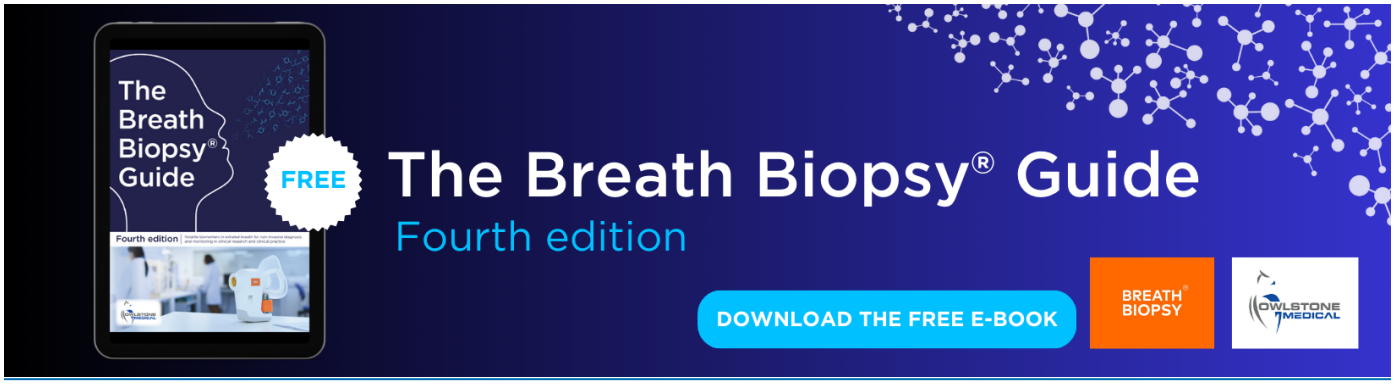

Materials Research Express

PAPER

Formation and stability of Fe-rich terminations of the $Fe_3O_4(001)$ surface

Oscar Gamba[1], **Moritz Eder**[2], **Matthias Poglitsch**[2], **Jiri Pavelec**[2], **Panukorn Sombut**[2], **Matthias Meier**[2], **Ulrike Diebold**[2], **Michael Schmid**[2] and **Gareth S Parkinson**[2,*]

[1] GeoRessources, Université de Lorraine, CNRS, 54000, Nancy, France
[2] Institute of Applied Physics, TU Wien, Vienna, Austria
[*] Author to whom any correspondence should be addressed.

E-mail: gareth.parkinson@tuwien.ac.at

OPEN ACCESS

RECEIVED
7 September 2023

REVISED
24 October 2023

ACCEPTED FOR PUBLICATION
8 November 2023

PUBLISHED
22 November 2023

Keywords: scanning tunneling microscopy, iron oxide surfaces, metal oxide surfaces, magnetite, x-ray photoelectron spectroscopy

Supplementary material for this article is available online

Abstract

Understanding how the structure of iron oxide surfaces varies with their environment is essential for rationalizing their role in (geo-)chemistry and optimizing their application in modern technologies. In this paper, we create Fe-rich terminations of $Fe_3O_4(001)$ by depositing iron directly onto the 'subsurface cation vacancy'-reconstructed surface, which is the most stable surface under ultrahigh vacuum conditions. Scanning tunneling microscopy and x-ray photoelectron spectroscopy data reveal that the excess iron is initially accommodated as two-fold coordinated adatoms and later incorporates into the subsurface cation vacancies. As the coverage increases, small patches of the octahedral pair termination (also known as the 'Fe dimer' termination) nucleate, eventually covering the entire surface after the deposition of 2 iron atoms per $(\sqrt{2}\times\sqrt{2})R45°$ unit cell. This conclusion effectively rules out some existing models for the termination and provides support for the model proposed by Rustad *et al* (Surface Science 432, L583-L588, 1999), highlighting the need for further theoretical work to complete the $Fe_3O_4(001)$ surface phase diagram. The octahedral pair termination is found to be unstable above 523 K and upon exposure to molecular O_2 because the excess iron atoms agglomerate to form small FeO_x clusters.

1. Introduction

Iron oxides are abundant minerals on Earth with a wide range of applications in magnetic devices [1], electronic materials [2, 3], biomedicine [4], and catalysis [5]. Since the atomic-scale structure of the surface ultimately defines its reactivity [6], there has been a long-standing effort to understand structure–function relationships at the atomic level using surface science techniques [7, 8]. Reduced surfaces are particularly interesting in the context of catalysis because catalysts are often activated by heating in CO or H_2 and applied at elevated temperatures in reducing environments.

Magnetite (Fe_3O_4) has been extensively studied in surface science experiments. This is partly because Fe_3O_4 is the active phase for the high-temperature water-gas shift reaction [9, 10] and because it is utilized as a reducible support for metal nanoparticles [11–13]. Moreover, Fe_3O_4 is well suited for experiments in ultrahigh vacuum (UHV) as it is the most stable iron oxide phase under UHV conditions [14] and high-quality samples can be readily purchased as single crystals or grown as thin films on metal substrates [7, 14]. Additionally, the material's half-metallicity [15] makes it amenable to analysis by electron-based techniques, including scanning tunneling microscopy (STM).

The most prominent facets of natural Fe_3O_4 crystals are (111) and (100). The (111) surface is terminated by a layer of tetrahedrally coordinated Fe atoms (Fe_{tet}) [16, 17], but patches with a different structure coexist and grow as the sample becomes reduced [18–21]. The structure of these patches is still debated [21, 22], but they exhibit different reactivity compared to the Fe_{tet} termination [21, 23, 24]. More extensive reduction of the

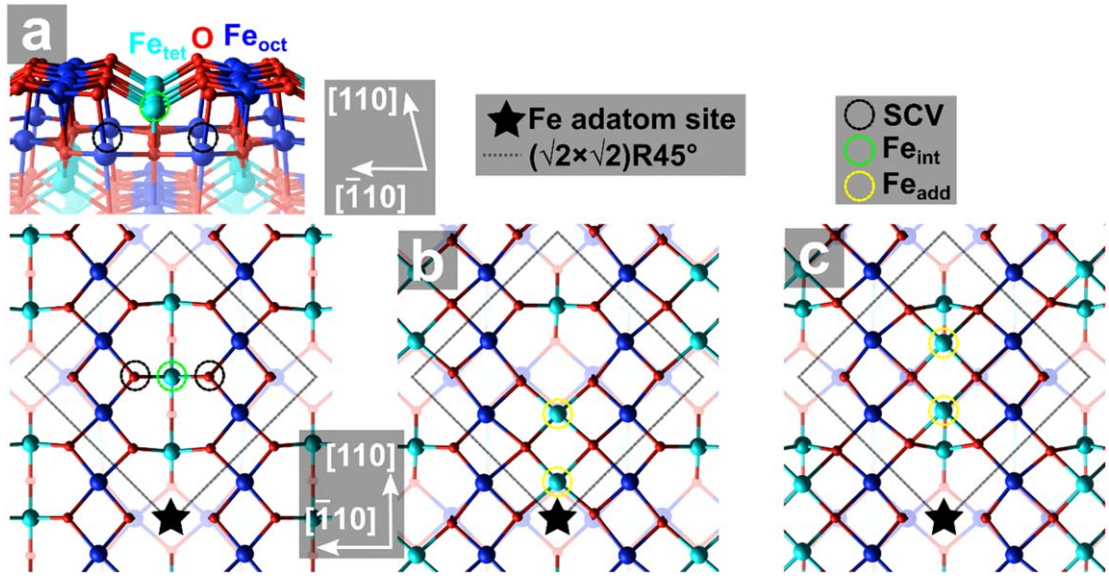

Figure 1. Models for the $Fe_3O_4(001)$ surface. (a) Perspective and top views of the subsurface cation vacancy (SCV) structure. Octahedrally coordinated Fe atoms (Fe_{oct}) are depicted in dark blue, tetrahedrally coordinated Fe atoms (Fe_{tet}) in cyan, and oxygen atoms in red. The positions of the subsurface Fe_{oct} vacancies are indicated by black circles, while the interstitial Fe atom (Fe_{int}) is marked with a green circle. In the top view, the black star denotes the typical adsorption site for metal adatoms within the reconstructed surface unit cell. (b) Top view of the structure proposed by Rustad *et al* [28], which contains two additional Fe atoms per unit cell compared to the SCV surface. The Fe atoms of the octahedral pair, also known as the Fe dimer, are highlighted in yellow. (c) Top view of the octahedral pair structure proposed by Novotny *et al* [32], which contains three additional Fe atoms per unit cell. The Fe atoms of the octahedral pair (Fe dimer) are highlighted in yellow.

sample leads to the observation of the so-called bi-phase termination [22, 25, 26], which precedes the full reduction of the sample selvedge to FeO.

The (001) facet exhibits a $(\sqrt{2}\times\sqrt{2})R45°$ periodicity when a sample is prepared under ultrahigh vacuum (UHV) conditions [27–29]. Empty-states STM images typically exhibit rows of protrusions running in <110>-type directions, consistent with the imaging of octahedral Fe atoms (Fe_{oct}) within an Fe_{oct}-O plane. The structure model for this surface, known as the subsurface cation vacancy (SCV) termination, is shown in figure 1(a). In each unit cell, two Fe_{oct} cations are removed from the third layer and replaced by an Fe_{tet} interstitial (Fe_{int}) in the second layer. This distorts the topmost surface layer, leading to undulations that are visible in STM images. The SCV model is supported by density functional theory (DFT) calculations [30], quantitative low-energy electron diffraction (LEED-IV) [30] and surface x-ray diffraction (SXRD) [31], and a predicted Fe^{3+} enrichment of the surface is observed in x-ray photoelectron spectroscopy (XPS) [30]. Furthermore, the SCV model is also consistent with the adsorption behaviour of various metal adatoms, as observed by STM: Adatoms occupy the specific site between two undercoordinated oxygen atoms marked by a black star in figure 1(a) [30, 46, 47]. In a truncated bulk structure, this site would be equivalent to the site marked by a green circle. In the reconstructed surface, the latter site is unfavourable due to the presence of the Fe_{int} atom.

Reduced terminations of $Fe_3O_4(001)$ have been reported on both bulk single-crystal samples and epitaxial thin films [17, 32–41]. Initially, a ½ ML Fe_{tet}-terminated surface was proposed [42] based on STM images showing protrusions between the surface Fe_{oct} rows. However, further STM investigations resolved the protrusions into pairs [35, 37, 40, 43–45], leading to this surface becoming known as the 'Fe dimer' termination of $Fe_3O_4(001)$. Previously, our group prepared this surface by depositing Fe directly onto the as-prepared $Fe_3O_4(001)$ surface at room temperature (RT). Based on STM data and DFT calculations, we determined that the Fe atoms constituting the 'dimer' are five-fold coordinated to surface oxygen atoms (see figure 1(c)), and that no Fe–Fe bond is formed [32]. We thus prefer the descriptor 'octahedral pair' to Fe dimer, and will utilize this terminology in what follows. Generally, these studies were conducted before the discovery of the SCV termination of $Fe_3O_4(001)$, and structural models of the octahedral pair do not take into account the possibility of subsurface rearrangements.

In this study, we revisit the experiments involving the deposition of Fe onto $Fe_3O_4(001)$ in light of the discovery of the SCV structure. Our investigation reveals that the octahedral pair termination requires an additional 2 Fe atoms per unit cell, which rules out various models found in the literature. We conclude that our observations align best with the structural model originally proposed by Rustad *et al* [28], and highlight the need for further theoretical study. Additionally, we explore the stability of Fe-rich surfaces. Our findings indicate that the additional Fe atoms are highly sensitive to trace O_2 in the environment, resulting in the formation of Fe_xO_y

clusters. Furthermore, we observe that Fe-rich terminations become unstable above 523 K as the excess Fe diffuses into the bulk.

2. Experimental details

STM and XPS experiments were conducted in a UHV system with a base pressure of $< 1 \times 10^{-10}$ mbar. The STM measurements were carried out at room temperature using an Omicron tripod-scanner STM with electrochemically etched W tips in constant current mode imaging empty states with a positive sample bias at 300 K. The images were processed to remove outlier pixels ('salt and pepper noise') by replacing them with the median of the adjacent pixels and corrected for distortions due to drift and creep of the piezo scanner [48]. XPS measurements were done using a non-monochromatic Al Kα x-ray source and a SPECS Phoibos 100 analyzer. Additional XPS measurements were conducted in a second chamber described in detail previously [49]. These measurements utilized a SPECS XR50M Al Kα x-ray source, a Focus 500 monochromator, and SPECS PHOIBOS 150 analyzer, which provided improved resolution. The trends observed in the measurements were identical in both chambers, and we thus show the high-resolution XPS results in this paper.

The samples used in the present work were Fe_3O_4(001) single crystals (6 mm×6 mm × 1 mm) of natural origin obtained from SurfaceNet GmbH. The crystals were mounted onto Ta sample plates using Ta clips, which uniformly press the sample at the periphery of the corners and are fixed by spot-welding to the Ta plate. A gold foil between sample and Ta plate ensured optimum heat conductivity. The sample was cleaned in UHV by 1 keV Ar^+ sputtering at room temperature for 20 min followed by annealing at 873 K for 15 min. Once no contamination could be detected by XPS in the C1*s* region, the sample was annealed in O_2 (5×10^{-7} mbar) at 873 K for 15 min. Annealing in O_2 leads to the growth of a pristine and uniform SCV reconstructed surface [50] with a low density of defects like domain boundaries [51], Fe adatoms or unreconstructed unit cells [52].

Fe was evaporated onto the Fe_3O_4 sample at room temperature from a 2 mm-thick rod (99.99+%, MaTeck GmbH) using an Omicron electron beam evaporator. The deposition rate was calibrated using a quartz crystal microbalance. One monolayer (ML) is defined as one atom per $(\sqrt{2}\times\sqrt{2})$R45° unit cell, which corresponds to 1.42×10^{14} atoms cm^{-2}.

3. Results

3.1. Fe deposition: from adatoms to the Fe octahedral pair surface

Figure 2 shows STM images of the Fe_3O_4(001) surface acquired after depositing different coverages of Fe onto the freshly prepared SCV reconstructed surface at room temperature. After deposition of 0.2 ML of Fe (figure 2(a)), the main new species are Fe adatoms [32]. These appear as single, bright protrusions between the Fe rows (some are highlighted by green ovals). The appearance of the Fe protrusions is similar to other metal adatoms such as Ag, Pd and Au [47, 53, 54], and is consistent with the adsorption site marked by a star in figure 1(a). The adatoms seem to be randomly distributed, but can be located in rather close proximity, often diagonally with respect to the Fe_{oct} rows. This suggests a preferential occupation of antiphase domain boundaries [51] in the SCV reconstruction. A second group of features, highlighted with yellow circles in figure 2(a), appear as a pair of protrusions located on opposite iron rows. By analogy with previous results obtained for the 3d transition metals Ni, Co, Ti, and Zr [46], we propose these result from the incorporation of an additional Fe atom in the subsurface layers. Specifically, the additional Fe atom occupies one of the subsurface Fe_{oct} vacancies of the SCV reconstruction, which then induces the Fe_{int} to move and occupy the neighbouring vacancy. This locally restores the bulk-like spinel structure. Hereafter, we refer to these defects as unreconstructed unit cells. Quantitatively, the total number of Fe adatoms amounts to 0.05–0.1 ML. The unreconstructed unit cells account for only a fraction of the 'missing' coverage, although determining their density is challenging due to their smeared-out appearance, especially if they are close to other protrusions. Nevertheless, the total number of observable Fe does not add up to 0.2 ML. This suggests that the (sub)surface can accommodate Fe in an additional site which is not observable by STM.

After deposition of 0.6 ML Fe (figure 2(b)), the number of adatom features remains approximately the same as for 0.2 ML. This again suggests adatoms may be stabilized at (sub)surface defects such as unreconstructed unit cells and antiphase domain boundaries, which has also been observed for low water and methanol coverages on Fe_3O_4(001) [52, 55]. In addition, a new configuration is observed in the STM images (red square): Small patches of protrusions located between the Fe rows with $(\sqrt{2}\times\sqrt{2})$R45° symmetry. These are lower in apparent height than the Fe adatoms, and can be resolved into two protrusions with a suitable STM tip [32]. These are the 'Fe dimers', or octahedral pairs, using our terminology. The apparent height of the neighbouring Fe_{oct} rows in this structure is higher than in the SCV reconstruction.

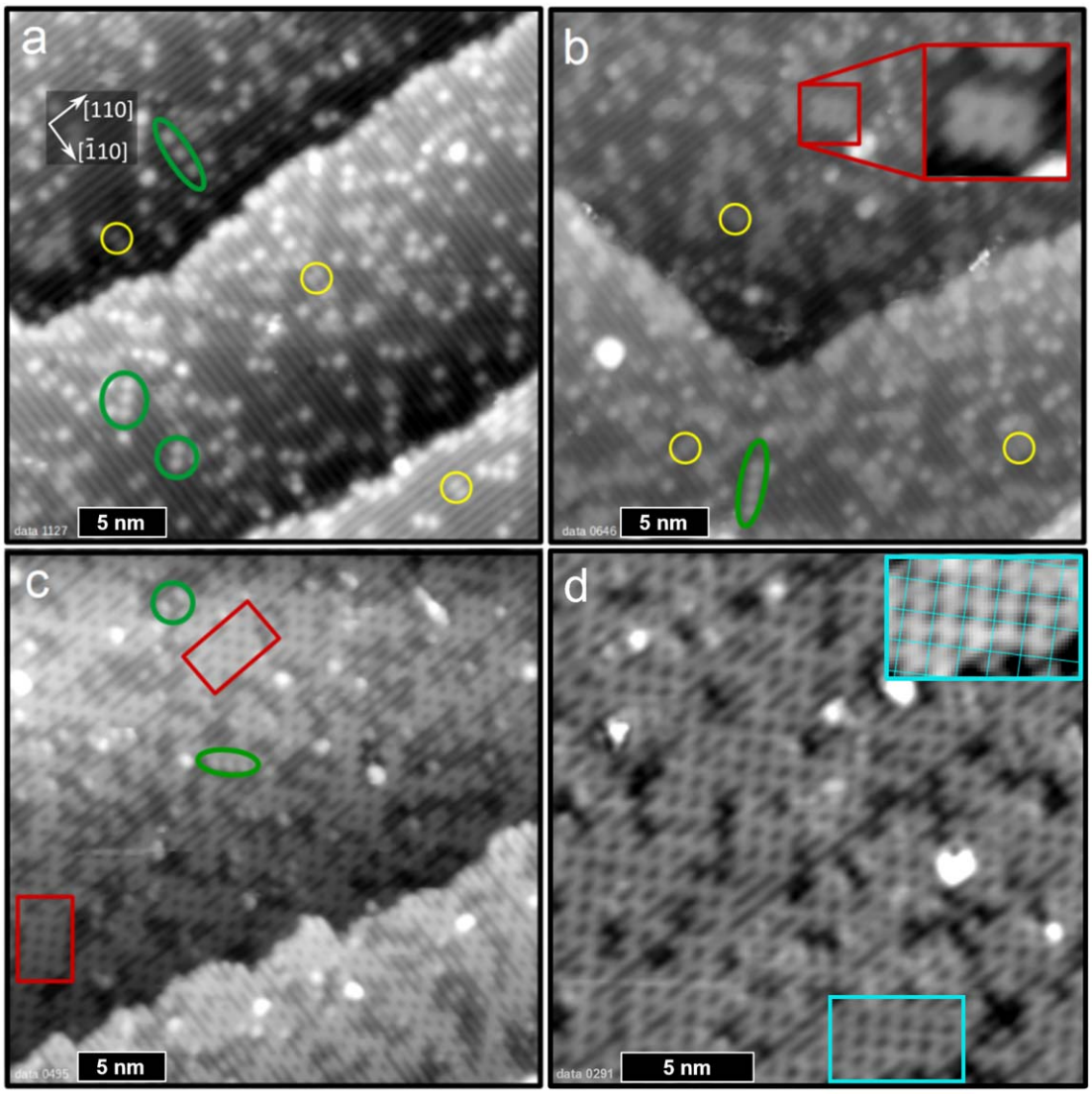

Figure 2. Room-temperature STM images (a-c: 30 × 30 nm^2, d: 20 × 20 nm^2) of different coverages of Fe on the Fe_3O_4(001) surface deposited and imaged at 300 K. Nominal Fe coverages are (a) 0.2 ML, (b) 0.6 ML, (c) 1 ML and (d) 2 ML. Fe initially adsorbs as adatoms (green ovals) and incorporate in the subsurface (yellow circles). At coverages of 0.6 ML and higher, Fe also forms areas with octahedral pairs (also named 'Fe dimers'; red rectangles), which dominate at high coverages. The $(\sqrt{2}\times\sqrt{2})R45°$ symmetry is highlighted in the inset with a cyan grid overlay. Tunneling conditions (sample voltage and tunneling currents): (a) +1.9 V/0.2 nA, (b) +1.7 V/0.3 nA, (c) +1.9 V/0.3 nA, (d) +1.5 V/0.3 nA.

After deposition of 1.0 ML (figure 2(c)), the unmodified SCV substrate remains visible in small patches, and approximately half of the surface unit cells are populated by octahedral pairs exhibiting a local $(\sqrt{2}\times\sqrt{2})R45°$ symmetry. Similar to the original SCV reconstruction, there are only a few antiphase domain boundaries in the $(\sqrt{2}\times\sqrt{2})R45°$ lattice of the octahedral pairs. This suggests that the octahedral pairs do not emerge from large (1 × 1) areas, i.e. a large patch of unreconstructed unit cells, because this would lead to the nucleation of random domains and an increased density of antiphase domain boundaries. Indeed, the small size of the patches of octahedral pairs suggest they form quickly once there are a few unreconstructed cells in close proximity. In some areas, single Fe adatoms coexist with octahedral pairs (green ovals in figure 2(c)) but the adatom density is still low (around 0.05 ML).

Figure 2(d) shows an STM image after deposition of 2 ML Fe onto the clean Fe_3O_4(001) surface. Here, the Fe octahedral pair structure dominates. The $(\sqrt{2}\times\sqrt{2})R45°$ symmetry is highlighted in the inset with a cyan grid overlay. Gaps visible in the structure are frequently associated with domain boundaries that were probably already present prior to Fe deposition. A small number of bright protrusions are also observed, which we previously attributed to Fe clusters [32]. In section 3.3, we will argue that these are Fe_xO_y clusters, which form due to a reaction of the Fe octahedral pairs and O_2 remaining in the residual gas after sample preparation.

The reduction of the surface due to Fe deposition (2 ML) is visible in XPS Fe2*p* and O1*s* core level spectra shown in figure 3. For the clean SCV reconstructed surface (black), the dominant contribution to the Fe

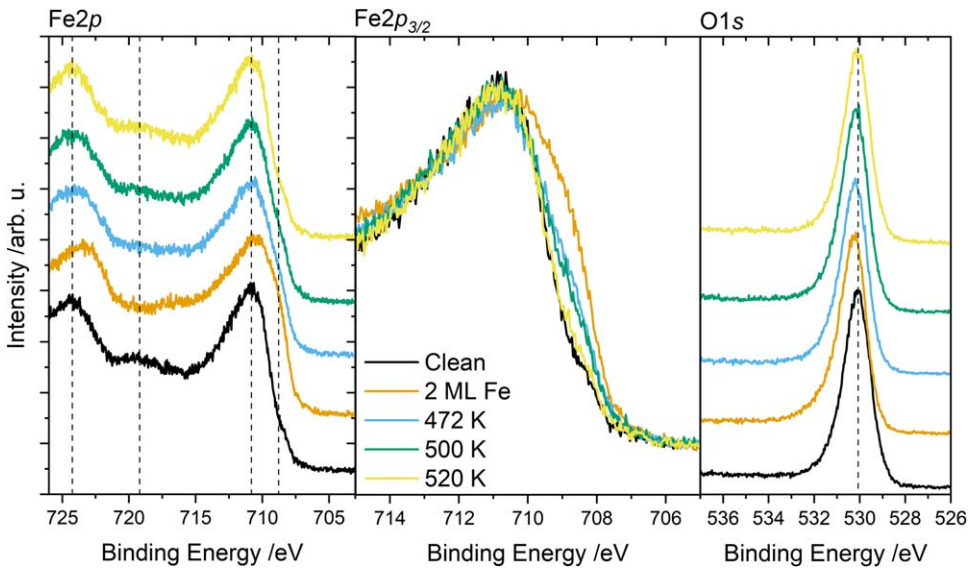

Figure 3. Fe*2p* and O*1s* XPS spectra comparing the SCV and octahedral pair terminations of Fe_3O_4(001). Spectra from the SCV reconstructed surface are coloured black, while those acquired following the deposition of 2 MLl Fe at 300 K are orange. Subsequently, a series of measurements were taken after heating to progressively higher temperatures to assess the thermal stability of the octahedral pair structure: 472 K (blue), 500 K (green), and 520 K (yellow). All measurements were conducted at 300 K.

spectrum comes from the Fe^{3+} cations, since this is the only oxidation state present in the four outermost layers [30]. The characteristic Fe^{3+}-related shake-up satellite peak is clearly present at ~718.5 eV. The surface dominated by Fe octahedral pairs (orange) exhibits an enhanced Fe^{2+} component at 708.7 eV, apparent as a shoulder in the Fe$2p_{3/2}$ peak, as well as increased intensity at the Fe^{2+}-related satellite peak at ≈715 eV [56–58]. The clean Fe_3O_4(001) surface exhibits a slightly asymmetric O1*s* peak at 530.1 eV due to the lattice oxygen in magnetite as reported previously [59–61]. For the octahedral Fe pair surface, the peak shifts 0.2 eV to higher binding energy and exhibits increased intensity in the range 532–533 eV.

3.2. Thermal stability of the Fe-rich surface

To evaluate the thermal stability of the Fe-rich surface, temperature-dependent XPS experiments were carried out. The Fe2*p* and O1*s* electron photoemission spectra were recorded after depositing 2 ML of Fe on the clean Fe_3O_4(001) surface and subsequently annealing to progressively higher temperatures (figure 3). Spectra were taken at room temperature after the sample had cooled down.

As the sample is annealed at progressively higher temperatures (blue, green and yellow), the intensity contribution from Fe^{2+} cations decreases (the shoulder around 708.7 eV and the satellite feature at 715 eV). After heating to 520 K, the spectra again resemble those for the SCV surface (black and yellow). Similarly, the O1*s* gradually shifts with higher temperature treatment (blue, green, and yellow) from the high binding energy position of the Fe octahedral pair surface (orange) to lower binding energies. After heating to 520 K, the lattice oxygen peak recovers its original position at 530.1 eV. These changes are related to the diffusion of the excess Fe into the bulk and the recovery of the SCV reconstruction [8]. This conclusion is consistent with STM results: The surface retains the octahedral pair configuration until 523 K, and annealing at higher temperature showed a characteristic Fe_3O_4(001)-($\sqrt{2}\times\sqrt{2}$)R45° surface (see SI figure 1).

3.3. Fe deposition at room temperature: effect of residual oxygen

In a previous study [32], we deposited Fe on Fe_3O_4(001) and observed a significant number of bright protrusions to coexist alongside the octahedral pair surface. At that time, we attributed these features to the build-up of metallic Fe that could not be accommodated in the surface [32]. In the course of this study, we initially observed such clusters already at very low coverages. By precisely controlling the amount of O_2 in the UHV chamber, it became evident that the clusters resulted from a reaction between deposited Fe atoms and residual O_2 present in the gas phase. While O_2 is not typically a major component of the residual gas, it occurs here as a consequence of the final oxidation treatment used to prepare a clean Fe_3O_4(001) surface (see section 2, Experimental Details). We demonstrate the effect of O_2 in figure 4. Figure 4(a) shows the Fe_3O_4(001) surface that results when Fe deposition was performed with 1×10^{-9} mbar O_2 intentionally leaked into the UHV chamber. Figure 4(b), in contrast, shows an STM image acquired after the same amount of Fe was deposited, but with several titanium sublimation pump (TSP) cycles run prior to Fe evaporation. The TSP is particularly effective for reducing the

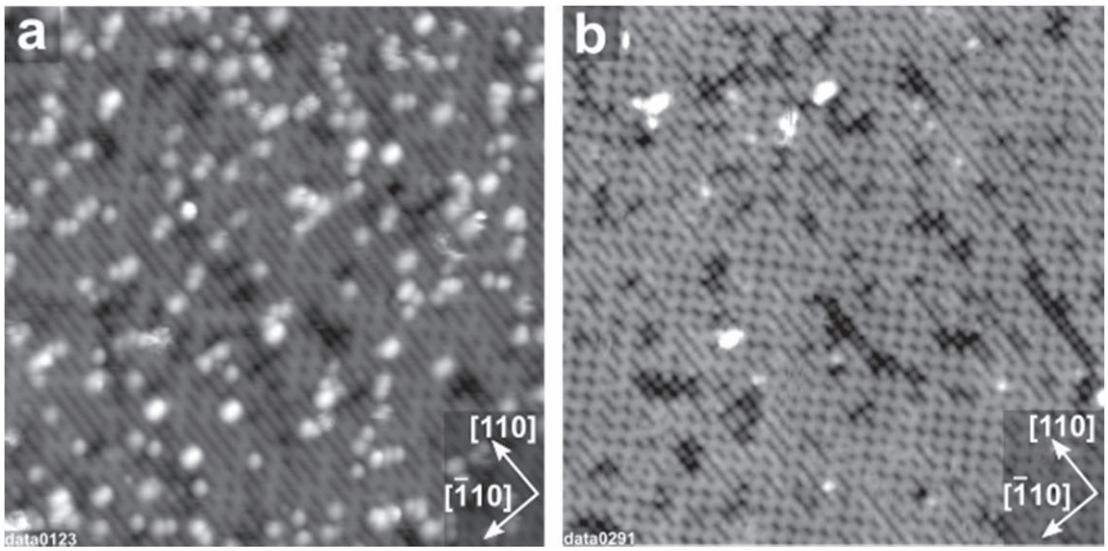

Figure 4. (a) STM image (27×27 nm^2, $V_{sample} = +1.5$ V, $I = 0.3$ nA) after deposition of 2 ML Fe at 300 K with O_2 in the background (1×10^{-9} mbar O_2 during deposition). (b) STM image (27×27 nm^2, $V_{sample} = +1.6$ V, $I = 0.3$ nA) after deposition of 2 ML Fe (deposition of Fe without oxygen after TSP cycles) at 300 K.

partial pressure of O_2 to well below 1×10^{-10} mbar. The density of bright protrusions in figure 4(b) is drastically reduced compared to figure 4(a). We find no evidence of metallic Fe in XPS in either case (see section 3.4) and we thus conclude that the bright protrusions are Fe_xO_y clusters formed through the oxidation of excess Fe by residual O_2. For the investigation of Fe surface species and octahedral pairs in figures 2–4, O_2 was always removed to the greatest possible extent prior to Fe deposition.

3.4. Fe-rich (001) surface: reactivity to oxygen

To investigate how the Fe_xO_y clusters formed, we prepared a surface containing Fe adatoms, unreconstructed unit cells, and patches of octahedral pairs (0.6 ML deposition, see figure 2(b)). We then recorded STM images on the same sample area while exposing the sample to 3×10^{-9} mbar of O_2. Figure 5 contains two panels (a and b) acquired from different regions of the surface. Each panel has six sequential frames from the STM movie. Panel (a) focuses on the behaviour of Fe adatoms. Between frame 1 and 4 (corresponding to a time span of 22 min), the surface features remained unchanged. In frame 5, the three adatoms near the Fe adatom labelled with the red circle are replaced by a cluster, which is indicated with the cyan arrow. No further changes are observed subsequently in frame 6.

In panel (b) of figure 5, the green square highlights a small patch of Fe octahedral pairs. Similar to Fe adatoms (figure 5(a)), the presence of oxygen leads to the formation of a cluster between frames 5 and 6. The phenomenon of adatom sintering induced by adsorbates has been observed previously for other metals on the Fe_3O_4(001) surface, for CO on Pd and Pt adatoms as well as for O_2 on Rh adatoms, where oxidized clusters (Rh_xO_y) were found [54, 62, 63].

The oxidation of the Fe-rich surface due to O_2 exposure is also evident in XPS. Figure 6 shows Fe2*p* (a) and O1*s* (b) core level spectra for the clean surface (black), the octahedral Fe pair surface (orange), after exposure to 10 Langmuir (L) of O_2 (blue), and subsequent annealing to 472 K (green) and 950 K (yellow). After the octahedral Fe pair surface is exposed to 10 L of O_2, the spectrum loses the Fe^{2+} component at 708.7 eV as well as the satellite peak at 715 eV, indicating the oxidation of Fe^{2+} to Fe^{3+}. For the O1*s* region, the lattice O peak recovers the position for the clean Fe_3O_4(001)-($\sqrt{2}\times\sqrt{2}$)R45° surface at 530.1 eV after O_2 exposure. Subsequent annealing to 472 K and 950 K does not induce any significant changes of the XPS spectra with respect to the oxidized surface.

4. Discussion

Evaporating Fe onto the Fe_3O_4(001) surface is an elegant way to steer the degree of reduction on iron oxide surfaces, effectively creating a model system in a more reduced environment. The results of this work suggest that Fe deposited onto Fe_3O_4(001) at room temperature can exist in three distinct configurations: At low coverages ($\leqslant 0.6$ ML), isolated Fe adatoms are present at a constant coverage of 0.05–0.1 ML. At higher coverage, deposited Fe moves to subsurface sites, which locally lifts the ($\sqrt{2}\times\sqrt{2}$)R45° reconstruction. The discrepancy

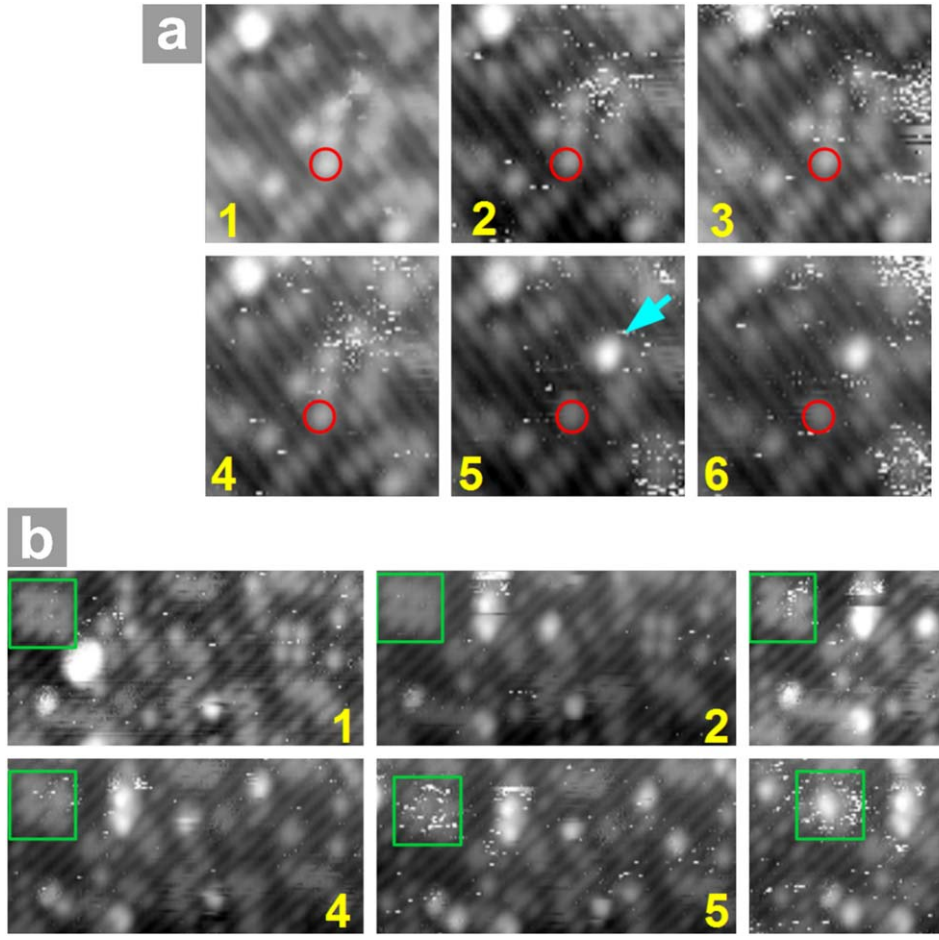

Figure 5. Imaging the effect of O_2 exposure on an Fe-rich $Fe_3O_4(001)$ surface. (a) Sequential frames from an STM movie (7.6 × 7.6 nm^2, $V_{sample} = +1.7$ V, I = 0.3 nA) acquired during exposure to 3×10^{-9} mbar O_2. The red circle in (a) marks the same adatom in all frames of (a). Between frames 4 and 5, four nearby Fe adatoms agglomerate and form an Fe_xO_y cluster (indicated b the cyan arrow). (b) Sequential frames selected from a different area of the same STM movie (7.6 × 7.6 nm^2, $V_{sample} = +1.7$ V, I = 0.3 nA). In this case, a small patch of the octahedral pair termination (green box) forms an Fe_xO_y cluster between frames 5 and 6.

between the amount of Fe deposited and the density of species observed suggests that there may be additional vacancies beneath the SCV reconstruction. This would not be surprising, because the sample is oxidized in the last step prior to Fe deposition, and it is known that this treatment leads to the growth of new $Fe_3O_4(001)$ layers using Fe supplied by the sample selvedge [50]. The amount of additional vacancies is in principle limited only by the eventual oxidation of all Fe^{2+} to Fe^{3+} and the formation of γ-Fe_2O_3 (maghemite). Both Fe_3O_4 and γ-Fe_2O_3 are based on the spinel structure, but γ-Fe_2O_3 has vacancies in the octahedral Fe sites.

As the coverage is increased, patches of octahedral pairs nucleate. After the deposition of 2 ML, the surface is almost entirely covered by octahedral pairs (figure 2). Although the nucleation mechanism cannot be directly derived from our results, the fact that the octahedral pairs initially appear in patches suggests a self-assisted growth, i.e. formation of one octahedral pair assists the formation of further pairs in its proximity. Moreover, isolated octahedral pairs were hardly observed, suggesting the process may actually require the neighbouring unit cell to also contain excess Fe.

The octahedral pair surface prepared by Fe deposition is not thermally stable, because the excess Fe diffuses into the bulk upon mild heating, leading to the recovery of the SCV reconstruction. It is likely that our oxidative treatment of the sample prior to Fe deposition contributes to this instability, because the sample selvedge will contain some degree of vacancies in the octahedral Fe lattice. As such, the degree of reduction and hence the termination of $Fe_3O_4(001)$ will always be a function of sample history. Bulk mobility of Fe in Fe_3O_4 already occurs around room temperature, but oxygen exchange between the sample and the gas phase is limited. This means that the termination of Fe_3O_4 surfaces is not only a function of the oxygen chemical potential applied during the final preparation step, as one might expect when viewing DFT-derived surface phase diagrams. This idea is consistent with the reports of stable Fe-rich terminations occurring on $Fe_3O_4(001)$ thin films that were grown on Fe buffer layers on MgO(100) [36] and Pt(100) [33]. The spinel lattice can also host excess Fe cations in interstitial sites, and it is likely that an Fe-rich sample bulk will be reflected in an Fe-rich termination. As the Fe

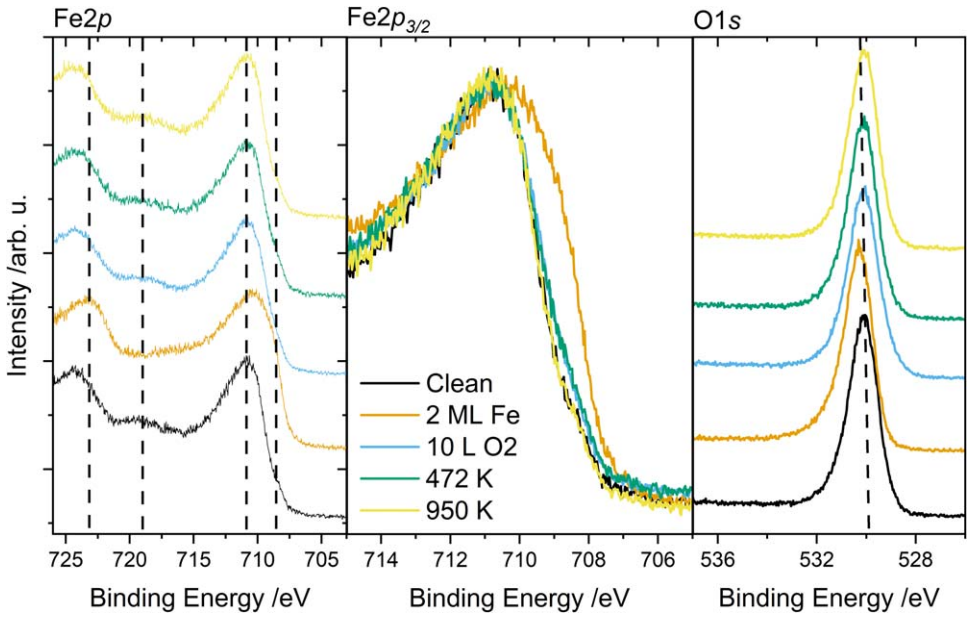

Figure 6. Fe*2p* and O*1s* XPS spectra acquired from the as-prepared Fe_3O_4(001)-($\sqrt{2} \times \sqrt{2}$)R45° SCV surface (black), and following the deposition of 2 ML Fe at 300 K (orange). Additional spectra show the effect of exposing the surface to 10 L O_2 (blue), and annealing to 472 K (green) and 950 K (yellow). All measurements were conducted at 300 K. The spectra are offset in the y-direction for clarity.

content is increased, Fe_{tet} cations are replaced by two Fe_{oct} cations until FeO stoichiometry is reached, and all Fe is Fe^{2+} in Fe_{oct} sites. FeO (wurtzite) and Fe_3O_4 (spinel) are based on a similar fcc oxygen lattice. Finally, we note that we have observed that performing many sputter/anneal cycles on single crystals without a post-oxidation step also leads to an Fe^{2+} rich surface that remains stable up to significantly higher temperature than observed here. Again, the Fe-rich sample selvedge leads to an Fe-rich termination at the surface.

One might think that the discussion above suggests that an Fe-rich sample of Fe_3O_4 could exhibit Fe-rich terminations even in relatively oxidizing conditions. However, our results suggest that this is probably not the case. Even at room temperature, exposure to small amounts of O_2 gas leads to the formation of small Fe_xO_y clusters. This hampered our attempts to create an ideal termination of octahedral Fe pairs in our previous study [32], and illustrates that the octahedral pair termination would not be stable in ambient conditions.

Finally, it is interesting to revisit the structure of the octahedral pair surface in the light of the discovery of the SCV structure. The fact that a saturation coverage of octahedral pairs is achieved at a coverage of 2 ML implies that this structure contains 2 additional Fe atoms per ($\sqrt{2}\times\sqrt{2}$)R45° unit cell. Thus, the model favoured in figure 3(c), which would require 3 additional atoms (one to lift the reconstruction, and another two for the octahedral Fe pair itself) is likely incorrect. Similarly, the model proposed in [36, 37] and computed in [64] is also ruled out as it features two additional Fe atoms on an otherwise bulk-truncated surface. One possible solution would be that the SCV reconstruction remains in the subsurface layers, and the two additional Fe atoms are simply accommodated on top of one surface unit cell. We consider the structure proposed by Rustad *et al* [28] to be more consistent with the coverage dependent behaviour observed here, because the octahedral pairs seem to form when additional Fe is added to a surface containing unreconstructed unit cells. In any case, our results suggest that an update of the Fe_3O_4(001) phase diagram in reducing conditions is required.

5. Conclusions

The octahedral Fe pair termination of Fe_3O_4(001) was prepared by evaporating Fe onto the Fe_3O_4(001)-($\sqrt{2}\times\sqrt{2}$)R45° surface at room temperature. At low coverage, excess Fe is accommodated as adatoms and via incorporation into the subsurface cation vacancies present in the SCV reconstruction. Adding two Fe atoms per ($\sqrt{2}\times\sqrt{2}$)R45° surface unit cell leads to a surface almost entirely covered in the octahedral Fe pair (previously called 'dimer') reconstruction. Fe-rich surfaces including a complete octahedral Fe pair termination are found to be unstable above 523 K under our conditions; excess Fe diffuses into the bulk leading to the recovery of the SCV reconstruction. Similarly, the octahedral pair termination is unstable in the presence of gaseous O_2 against the formation of small iron oxide clusters.

Acknowledgments

GSP, MM, UD, and MS were supported by the Austrian Science Fund (FWF) under project number F81, Taming Complexity in Materials Modeling (TACO). GSP, MM, JP, and PS acknowledge funding from the European Research Council (ERC) under the European Union's Horizon 2020 research and innovation programme (grant agreement No. [864628], Consolidator Research Grant 'E-SAC'). ME and GSP acknowledges funding from the EU Marie Skłodowska-Curie Actions of Horizon-MSCA-2022-PF-01 (Project 101103731 — SCI-PHI) and the COST action COSY, supported by COST (European Cooperation in Science and Technology).

Data availability statement

All data that support the findings of this study are included within the article (and any supplementary files).

ORCID iDs

Oscar Gamba https://orcid.org/0000-0002-3177-1620
Panukorn Sombut https://orcid.org/0000-0002-9372-9380
Gareth S Parkinson https://orcid.org/0000-0003-2457-8977

References

[1] Ajinkya N, Yu X, Kaithal P, Luo H, Somani P and Ramakrishna S 2020 Magnetic iron oxide nanoparticle (IONP) synthesis to applications: present and future *In Materials* **13** 4644
[2] Xia Q, Xu M, Xia H and Xie J 2016 Nanostructured iron oxide/hydroxide-based electrode materials for supercapacitors *ChemNanoMat* **2** 588–600
[3] Gleitzer C 1996 Electrical properties of anhydrous iron oxides *Key Eng. Mater.* **125** 355–418
[4] Attia N F, El-Monaem E M A, El-Aqapa H G, Elashery S E A, Eltaweil A S, El Kady M, Khalifa S A M, Hawash H B and El-Seedi H R 2022 Iron oxide nanoparticles and their pharmaceutical applications *Applied Surface Science Advances* **11** 100284
[5] Hasany S F, Abdurahman N H, Sunarti A R and Jose R 2013 Magnetic iron oxide nanoparticles: chemical synthesis and applications review *Current Nanoscience* **9** 561–75
[6] Zhu N, Ji H, Yu P, Niu J, Farooq M U, Akram M W, Udego I O, Li H and Niu X 2018 Surface modification of magnetic iron oxide nanoparticles *Nanomaterials* **8** 810
[7] Kuhlenbeck H, Shaikhutdinov S and Freund H-J 2013 Well-ordered transition metal oxide layers in model catalysis—A series of case studies *Chem. Rev.* **113** 3986–4034
[8] Parkinson G S 2016 Iron oxide surfaces *Surf. Sci. Rep.* **71** 272–365
[9] Liu X, Ma Z, Meng Y, Ma Y-J and Wen X-D 2021 First-principles study on the mechanism of water-gas shift reaction on the Fe_3O_4 (111)-Fe_{tet1} *Molecular Catalysis* **516** 111998
[10] Zhu M and Wachs I E 2016 Iron-based catalysts for the high-temperature water–gas shift (HT-WGS) reaction: a review *ACS Catal.* **6** 722–32
[11] Liu M, Ye Y, Ye J, Gao T, Wang D, Chen G and Song Z 2023 Recent advances of magnetite (Fe_3O_4)-based magnetic materials in catalytic applications *Magnetochemistry* **9** 110
[12] Qin Z H, Lewandowski M, Sun Y N, Shaikhutdinov S and Freund H J 2008 Encapsulation of Pt nanoparticles as a result of strong metal −support interaction with Fe_3O_4 (111) *J. Phys. Chem.* C **112** 10209–13
[13] Kaiser S, Maleki F, Zhang K, Harbich W, Heiz U, Tosoni S, Lechner B A J, Pacchioni G and Esch F 2021 Cluster catalysis with lattice oxygen: tracing oxygen transport from a magnetite (001) support onto small Pt clusters *ACS Catal.* **11** 9519–29
[14] Ketteler G, Weiss W, Ranke W and Schlögl R 2001 Bulk and surface phases of iron oxides in an oxygen and water atmosphere at low pressure *Phys. Chem. Chem. Phys.* **3** 1114–22
[15] Wang W *et al* 2013 Fe t_{2g} band dispersion and spin polarization in thin films of Fe_3O_4(0 0 1)/MgO(0 0 1): half-metallicity of magnetite revisited *Phys. Rev.* B **87** 085118
[16] Sala A, Marchetto H, Qin Z H, Shaikhutdinov S, Schmidt T and Freund H J 2012 Defects and inhomogeneities in Fe_3O_4(111) thin film growth on Pt(111) *Phys. Rev.* B **86** 155430
[17] Zaki E, Jakub Z, Mirabella F, Parkinson G S, Shaikhutdinov S and Freund H-J 2019 Water ordering on the magnetite Fe_3O_4 surfaces *J. Phys. Chem. Lett.* **10** 2487–92
[18] Wojas J, Kwiatek N, Wilgocka-Ślęzak D, Madej E, Korecki J and Spiridis N 2020 CO adsorption on Fe_3O_4(1 1 1) with regular and biphase terminations *Appl. Surf. Sci.* **507** 145069
[19] Creutzburg M, Sellschopp K, Gleißner R, Arndt B, Vonbun-Feldbauer G B, Vonk V, Noei H and Stierle A 2022 Surface structure of magnetite (111) under oxidizing and reducing conditions *J. Phys. Condens. Matter* **34** 164003
[20] Shimizu T K, Jung J, Kato H S, Kim Y and Kawai M 2010 Termination and Verwey transition of the (111) surface of magnetite studied by scanning tunneling microscopy and first-principles calculations *Phys. Rev.* B **81** 235429
[21] Kraushofer F, Meier M, Jakub Z, Hütner J, Balajka J, Hulva J, Schmid M, Franchini C, Diebold U and Parkinson G S 2023 Oxygen-terminated (1 × 1) reconstruction of reduced magnetite Fe_3O_4(111) *J. Phys. Chem. Lett.* **14** 3258–65
[22] Spiridis N, Freindl K, Wojas J, Kwiatek N, Madej E, Wilgocka-Ślęzak D, Dróżdż P, Ślęzak T and Korecki J 2019 Superstructures on epitaxial Fe_3O_4(111) films: biphase formation versus the degree of reduction *J. Phys. Chem.* C **123** 4204–16
[23] Mirabella F, Zaki E, Ivars-Barceló F, Li X, Paier J, Sauer J, Shaikhutdinov S and Freund H-J 2018 Cooperative formation of long-range ordering in water Ad-layers on Fe_3O_4(111) surfaces *Angew. Chem. Int. Ed.* **57** 1409–13
[24] Cutting R S, Muryn C A, Thornton G and Vaughan D J 2006 Molecular scale investigations of the reactivity of magnetite with formic acid, pyridine, and carbon tetrachloride *Geochim. Cosmochim. Acta* **70** 3593–612

[25] Liu Y, Wu Z, Naschitzki M, Gewinner S, Schöllkopf W, Li X, Paier J, Sauer J, Kuhlenbeck H and Freund H-J 2020 Elucidating surface structure with action spectroscopy *J. Am. Chem. Soc.* **142** 2665–71

[26] Condon N G, Leibsle F M, Parker T, Lennie A R, Vaughan D J and Thornton G 1997 Biphase ordering on Fe_3O_4(111) *Phys. Rev.*B **55** 15885–94

[27] Stanka B, Hebenstreit W, Diebold U and Chambers S A 2000 Surface reconstruction of Fe_3O_4(001) *Surf. Sci.* **448** 49–63

[28] Rustad J R, Wasserman E and Felmy A R 1999 A molecular dynamics investigation of surface reconstruction on magnetite (001) *Surf. Sci.* **432** L583–8

[29] Pentcheva R, Wendler F, Meyerheim H L, Moritz W, Jedrecy N and Scheffler M 2005 Jahn-Teller stabilization of a 'Polar' metal oxide surface: Fe_3O_4(001) *Phys. Rev. Lett.* **94** 126101

[30] Bliem R *et al* 2014 Subsurface cation vacancy stabilization of the magnetite (001) *Science* **346** 1215–8

[31] Arndt B, Bliem R, Gamba O, van der Hoeven J E S, Noei H, Diebold U, Parkinson G S and Stierle A 2016 Atomic structure and stability of magnetite Fe_3O_4(001): An x-ray view *Surf. Sci.* **653** 76–81

[32] Novotny Z, Mulakaluri N, Edes Z, Schmid M, Pentcheva R, Diebold U and Parkinson G S 2013 Probing the surface phase diagram of Fe_3O_4(001) towards the Fe-rich limit: Evidence for progressive reduction of the surface *Phys. Rev.*B **87** 195410

[33] Davis E M, Zhang K, Cui Y, Kuhlenbeck H, Shaikhutdinov S and Freund H-J 2015 Growth of Fe_3O_4(001) thin films on Pt(100): Tuning surface termination with an Fe buffer layer *Surf. Sci.* **636** 42–6

[34] Spiridis N, Handke B, Slezak T, Barbasz J, Zajac M, Haber J and Korecki J 2004 Surface structure of epitaxial magnetite Fe_3O_4(001) films: *In Situ* STM and CEMS studies *J. Phys. Chem.* B **108** 14356–61

[35] Parkinson G S, Novotný Z, Jacobson P, Schmid M and Diebold U 2011 A metastable Fe(A) termination at the Fe_3O_4(001) surface *Surf. Sci.* **605** L42–5

[36] Spiridis N, Barbasz J, Łodziana Z and Korecki J 2006 Fe_3O_4(001) films on Fe(001): Termination and reconstruction of iron-rich surfaces *Phys. Rev.* B **74** 155423

[37] Spiridis N, Madej E and Korecki J 2014 Adsorption of gold on an iron-rich Fe_3O_4(001) surface *J. Phys. Chem.* C **118** 2011–7

[38] Chambers S A and Joyce S A 1999 Surface termination, composition and reconstruction of Fe_3O_4(001)and γ-Fe_2O_3(001) *Surf. Sci.* **420** 111–22

[39] Kim Y J, Gao Y and Chambers S A 1997 Selective growth and characterization of pure, epitaxial α-Fe_2O_3(0001) and Fe_3O_4(001) films by plasma-assisted molecular beam epitaxy *Surf. Sci.* **371** 358–70

[40] Gaines J M *et al* 1997 An STM study of Fe_3O_4(100) grown by molecular beam epitaxy *Surf. Sci.* **373** 85–94

[41] Zhang K, Shaikhutdinov S and Freund H-J 2015 Does the surface structure of oxide affect the strong metal–support interaction with platinum? Platinum on Fe_3O_4(001) versus Fe_3O_4(111) *ChemCatChem* **7** 3725–30

[42] Chambers S A, Thevuthasan S and Joyce S A 2000 Surface structure of MBE-grown Fe_3O_4(001) by x-ray photoelectron diffraction and scanning tunneling microscopy *Surf. Sci.* **450** L273–9

[43] Tarrach G, Bürgler D, Schaub T, Wiesendanger R and Güntherodt H J 1993 Atomic surface structure of Fe_3O_4(001) in different preparation stages studied by scanning tunneling microscopy *Surf. Sci.* **285** 1–14

[44] Gaines J M, Kohlhepp J T, van Eemeren J T W M, Elfrink R J G, Roozeboom F and de Jonge W J M 1997 The (001) surface of Fe_3O_4 grown epitaxially on MgO and characterized by scanning tunneling microscopy *MRS Proc.* **474** 191

[45] Ceballos S F, Mariotto G, Jordan K, Murphy S, Seoighe C and Shvets I V 2004 An atomic scale STM study of the Fe_3O_4(001) surface *Surf. Sci.* **548** 106–16

[46] Bliem R *et al* 2015 Adsorption and incorporation of transition metals at the magnetite Fe_3O_4(001) surface *Phys. Rev.*B **92** 075440

[47] Bliem R *et al* 2014 Cluster nucleation and growth from a highly supersaturated adatom phase: silver on magnetite *ACS Nano* **8** 7531–7

[48] Choi J I J, Mayr-Schmölzer W, Mittendorfer F, Redinger J, Diebold U and Schmid M 2014 The growth of ultra-thin zirconia films on Pd_3Zr(0001) *J. Phys. Condens. Matter* **26** 225003

[49] Pavelec J, Hulva J, Halwidl D, Bliem R, Gamba O, Jakub Z, Brunbauer F, Schmid M, Diebold U and Parkinson G S 2017 A multi-technique study of CO_2 adsorption on Fe_3O_4 magnetite *J. Chem. Phys.* **146** 014701

[50] Nie S, Starodub E, Monti M, Siegel D A, Vergara L, El Gabaly F, Bartelt N C, de la Figuera J and McCarty K F 2013 Insight into Magnetite's redox catalysis from observing surface morphology during oxidation *J. Am. Chem. Soc.* **135** 10091–8

[51] Parkinson G S, Manz T A, Novotný Z, Sprunger P T, Kurtz R L, Schmid M, Sholl D S and Diebold U 2012 Antiphase domain boundaries at the Fe_3O_4(001) surface *Phys. Rev.*B **85** 195450

[52] Gamba O, Hulva J, Pavelec J, Bliem R, Schmid M, Diebold U and Parkinson G S 2017 The role of surface defects in the adsorption of methanol on Fe_3O_4(001) *Top. Catal.* **60** 420–30

[53] Novotný Z, Argentero G, Wang Z, Schmid M, Diebold U and Parkinson G S 2012 Ordered array of single adatoms with remarkable thermal stability: Au/Fe_3O_4(001) *Phys. Rev. Lett.* **108** 216103

[54] Parkinson G S, Novotny Z, Argentero G, Schmid M, Pavelec J, Kosak R, Blaha P and Diebold U 2013 Carbon monoxide-induced adatom sintering in a Pd–Fe_3O_4 model catalyst *Nat. Mater.* **12** 724–8

[55] Meier M, Hulva J, Jakub Z, Pavelec J, Setvin M, Bliem R, Schmid M, Diebold U, Franchini C and Parkinson G S 2018 Water agglomerates on Fe_3O_4(001) *Proc. Natl Acad. Sci.* **115** E5642–50

[56] Yamashita T and Hayes P 2008 Analysis of XPS spectra of Fe^{2+} and Fe^{3+} ions in oxide materials *Appl. Surf. Sci.* **254** 2441–9

[57] Biesinger M C, Payne B P, Grosvenor A P, Lau L W M, Gerson A R and Smart R S C 2011 Resolving surface chemical states in XPS analysis of first row transition metals, oxides and hydroxides: Cr, Mn, Fe, Co and Ni *Appl. Surf. Sci.* **257** 2717–30

[58] Lin T-C, Seshadri G and Kelber J A 1997 A consistent method for quantitative XPS peak analysis of thin oxide films on clean polycrystalline iron surfaces *Appl. Surf. Sci.* **119** 83–92

[59] Taguchi M *et al* 2015 Temperature dependence of magnetically active charge excitations in magnetite across the Verwey transition *Phys. Rev. Lett.* **115** 256405

[60] Mirabella F, Balajka J, Pavelec J, Göbel M, Kraushofer F, Schmid M, Parkinson G S and Diebold U 2020 Atomic-scale studies of Fe_3O_4(001) and TiO_2(110) surfaces following immersion in CO_2-acidified water *ChemPhysChem* **21** 1788–96

[61] Anderson J F, Kuhn M and Diebold U 1996 Epitaxially grown Fe_3O_4 thin films: an XPS study *Surf. Sci. Spectra* **4** 266–72

[62] Bliem R, van der Hoeven J E S, Hulva J, Pavelec J, Gamba O, de Jongh P E, Schmid M, Blaha P, Diebold U and Parkinson G S 2016 Dual role of CO in the stability of subnano Pt clusters at the Fe_3O_4(001) surface *Proc. Natl. Acad. Sci.* **113** 8921–6

[63] Jakub Z *et al* 2020 Adsorbate-induced structural evolution changes the mechanism of CO oxidation on a Rh/Fe_3O_4(001) model catalyst *Nanoscale* **12** 5866–75

[64] Łodziana Z 2007 Surface Verwey transition in magnetite *Phys. Rev. Lett.* **99** 206402